ELSEVIER

Journal of Fluids and Structures 20 (2005) 893–912

JOURNAL OF FLUIDS AND STRUCTURES

www.elsevier.com/locate/jfs

Instability of a cantilevered flexible plate in viscous channel flow

T.S. Balint[a], A.D. Lucey[b,*]

[a]*Jet Propulsion Laboratory, California Institute of Technology, USA*
[b]*Department of Mechanical Engineering, Curtin University of Technology, P.O. Box U1987, Perth 6845, Australia*

Received 6 August 2004; accepted 13 May 2005

Abstract

The stability of a flexible cantilevered plate in viscous channel flow is studied as a representation of the dynamics of the human upper airway. The focus is on instability mechanisms of the soft palate (flexible plate) that cause airway blockage during sleep. We solve the Navier–Stokes equations for flow with Reynolds numbers up to 1500 fully coupled with the dynamics of the plate motion solved using finite-differences. The study is 2-D and based upon linearized plate mechanics. When both upper and lower airways are open, the plate is found to lose its stability through a *flutter* mechanism and a critical Reynolds number exists. When one airway is closed, the plate principally loses its stability through a *divergence* mechanism and a critical flow speed exists. However, below the divergence-onset flow speed, flutter can exist for low levels of structural damping in the flexible plate. Our results serve to extend understanding of flow-induced instability of cantilevered flexible plates and will ultimately improve the diagnosis and treatment of upper-airway disorders.

Keywords: Cantilevered flexible plate; Flutter; Divergence instability; Upper-airway disorder; Channel flow

1. Introduction

The work of this paper is principally motivated by the need to understand the pathology of human upper-airway impairment that causes the conditions of snoring and Obstructive Sleep Apnoea/Hypopnea (OSAH). Although, snoring sounds are often regarded lightheartedly, they may signal the occurrence of airway collapse, a severe condition afflicting an estimated 2–4% of the adult population (Young et al., 1992). Repeated airway-collapse, with associated arousal from sleep, can cause dangerous levels of daytime drowsiness, leading to lost productivity and, at worst, workplace accidents. Other snores indicate less severe consequences, but remain disabling for sufferers who number some 60% and 17%, respectively, of the male and female adult population. Fig. 1(a) shows an anatomical sketch of the upper-airway, or pharyngeal, region identifying the soft palate, a flexible flap of tissue, and the pharynx, a channel with flexible walls. Snoring sounds occur as a consequence of flutter-type motions of the soft palate (Huang, 1995) while complete airway blockage is associated with collapse of the pharyngeal channel (Huang and Ffowcs Williams, 1999; Pierce and Worsnop, 1999). However, recent measurements suggest that soft-palate motion is implicated in the process of airway

*Corresponding author. Tel.: +61 8 9266 7047; fax: +61 8 9266 2681.
E-mail address: a.lucey@curtin.edu.au (A.D. Lucey).

0889-9746/$ - see front matter
doi:10.1016/j.jfluidstructs.2005.05.005

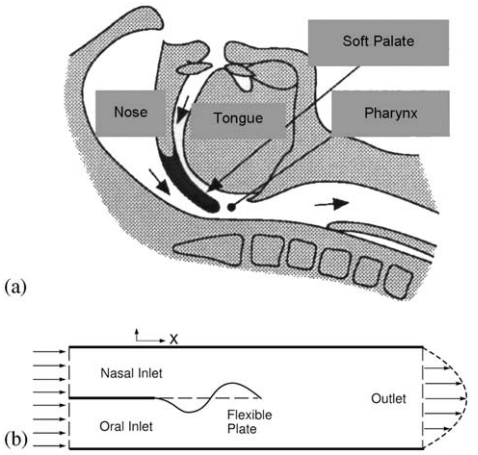

Fig. 1. (a) Sagittal view of upper-airway system [adapted from Aurégan and Depollier (1995)], and (b) schematic of analogue mechanical model.

blockage as opposed to the mechanism being purely the Starling-resistor type of tube collapse suggested, for example, by Aittokallio et al. (2001).In particular, OSAH appears more likely to occur when there is an extreme imbalance of air-flow rate between nasal and oral channels. Nevertheless, the mechanism for airway blockage—tube-collapse or blockage—remains an open question and, indeed, may vary from individual to individual. The present paper focuses on air-flow in a rigid-walled channel in which is mounted a thin cantilevered flexible plate attached to an upstream rigid plate; these elements, respectively, represent the pharynx, soft palate and hard palate. The mechanical system studied is schematically shown in Fig. 1(b). We investigate two distinct cases, these being (i) both upper and lower (nasal and oral) inlets open, and (ii) only one inlet open. For the latter case, we identify an instability mechanism that could lead to airway blockage without significant flow–structure interaction of channel structure. This case represents the most extreme imbalance between nasal and oral flow rates. Our goal is to elucidate instability mechanisms as opposed to conducting a quantitative investigation of instabililty bounds for the system. Although motivated by a biomechanical application, we remark that the system studied is one of fundamental interest in flow–structure interaction.

The system shown in Fig. 1(b) has most commonly been studied by assuming incompressible potential flow. Kornecki et al. (1976) conducted theoretical and experimental investigations of flexible plates for both two-fixed-ends and a cantilevered configuration in an unbounded fluid domain. Divergence was predicted for a plate with both ends fixed and flutter for a cantilevered configuration. Divergence occurs when the hydrodynamic force generated by a structure's deformation exceeds its restorative forces whereas flutter-type instabilities do not involve a force balance but require a phase shift between the hydrodynamic forces and the movement of the structural boundary. This provides a mechanism for irreversible energy transfer into the structure from the mean-flow kinetic energy. Huang (1995) and Huang and Ffowcs Williams (1999) investigated stability bounds and flutter for flow past a cantilevered elastic plate in an infinite domain with corresponding experimental work conducted in a 2-D channel. Snoring (flutter) was modelled using a linear analysis of plate motion with in vacuo modes, written as a truncated sum of orthogonal functions, used to approximate the deformation of the fluid-loaded plate. Although purely potential flow was used, viscous effects were implicitly included through a Kutta condition at the free trailing edge. Guo and Païdoussis (2000) conducted a theoretical study of the instability of thin elastic plates in plane-channel potential flow. Plate deformation was again written in the form of orthogonal beam functions and the flow–structure system solved using a Galerkin technique. Broadly, plates with a free end were found to lose their stability through flutter while those with both ends fixed first succumbed to divergence as the applied flow speed was increased. Previously Aurégan and Depollier (1995) had studied the same problem as Guo and Païdoussis but neglecting plate curvature; flutter occurred through blockage effects arising from the motion of the flexible plate.

Collectively, the inviscid-flow studies described immediately above evidence three types of instability. In the absence of channel walls, a flexible plate with a downstream free end flutters because its finiteness yields aerodynamic forces that are out-of-phase with its motion—the Huang (1995) flutter. In a channel, the same plate may flutter because its motion alternatively reduces and increases the half-channel width above and below it. The resulting forces from the ensuing Bernoulli-effect are out of phase with plate motion thereby generating the flutter of Aurégan and Depollier (1995).

Finally, a flexible plate may diverge due simply to the magnitude of the destabilizing aerodynamic forces, as shown by Guo and Païdoussis (2000) for panels with fixed ends.

The key development of the work presented in this paper is that viscous effects in the flow are fully incorporated. In the upper airway, relatively low Reynolds-number flow prevails. Thus, we model unsteady laminar flow, while retaining the use of thin-plate mechanics to model the soft palate. However, the use of simulation in the present work permits arbitrary deformations of the flexible plate to be accommodated and allows the development of unstable behaviour to be studied as an initial-value problem. Our present computational model also permits the investigation of the most extreme case of asymmetry between the upper (oral) and lower (nasal) inlet channels. Our objective is to identify instability mechanisms of the flow–structure system as opposed to providing a detailed quantitative investigation. In doing so, we reveal both flutter- and divergence-type instabilities, the interplay of these instabilities and their dependence upon channel configuration. Clearly, our system remains significantly different from that of the actual upper airway because finite-width and channel-curvature effects are neglected; thus, in the concluding remarks of Section 4 we consider the mean-flow field in a channel that more realistically represents the upper-airway system.

2. Computational modelling

2.1. Plate mechanics

The motion of the plate, driven by a pressure field is modelled using classical thin-plate mechanics. The plate's motion is driven by pressure fields $\delta p_U(x)$ and $\delta p_L(x)$, respectively, over its upper and lower surfaces. Vertical displacement, $w(x,t)$, is therefore governed by

$$m\ddot{w} + d\dot{w} + Bw_{,xxxx} = -(\delta p_U - \delta p_L) = -\Delta p, \tag{1}$$

where m and B are, respectively, the plate's specific mass and flexural rigidity defined by

$$m = \rho_m h \quad \text{and} \quad B = Eh^3/[12(1-\nu^2)],$$

where E, ν and ρ_m are, respectively, the elastic modulus, Poisson ratio and density of the plate material while h is the plate thickness. We allow for the inclusion of damping effects through dashpot damping with coefficient d, noting that this simple form is used only to examine the qualitative effects of plate-energy dissipation. Built-in boundary conditions are enforced at the plate's upstream end while at its trailing edge the conditions of zero shear and bending moment are applied. Thus for a plate of streamwise length L, we have

$$w(0,t) = w_{,x}(0,t) = 0 \quad \text{and} \quad w_{,xx}(L,t) = w_{,xxx}(L,t) = 0. \tag{2a,b}$$

Eq. (1) is solved using the finite-difference scheme described in Lucey et al. (1997) that incorporates an implicit time-stepping algorithm. In that study, the flexible plate had fixed hinged connections at both of its leading and trailing edges. For the present cantilevered configuration the clamped leading-edge condition corresponding to Eq. (2a) requires that

$$w_0 = w_1 = 0 \tag{3}$$

for plate deflections w_i at the equidistantly spaced mass points, $i = 0 \to N$ over the spatial range $x = 0 \to L$. The free-end conditions are enforced by evaluating the flexure term, $Bw_{,xxxx}$, at w_N using two dummy nodes, $N+1$ and $N+2$, beyond the end of the plate, whose displacements are found from the equations

$$w_{N+1} = 2w_N - w_{N-1} \quad \text{and} \quad w_{N+2} = 3w_N - 2w_{N-1}, \tag{4a,b}$$

that are obtained from the discretized form Eq. (2b) as described in Balint (2001).

The numerical model has been tested through simulations of undamped plate motion in vacuo associated with the first six eigenmodes. In order to do this we set $\Delta p = 0$ and $d = 0$ in Eq. (1). From Nowcaki (1963), the nth eigenfunction, w_n^*, is given by

$$w_n^*(x) = C\left[U(\lambda_n x) - \frac{S(\beta_n)}{T(\beta_n)}\, V(\lambda_n x)\right], \tag{5}$$

where C is an (amplitude) scaling constant, and V, U, T and S are defined as

$$V(\lambda_n x) = \frac{\sinh(\lambda_n x) - \sin(\lambda_n x)}{2}, \quad U(\lambda_n x) = \frac{\cosh(\lambda_n x) - \cos(\lambda_n x)}{2},$$

$$T(\beta_n) = \frac{\sinh\,\beta_n + \sin\,\beta_n}{2}, \quad S(\beta_n) = \frac{\cosh\,\beta_n + \cos\,\beta_n}{2}$$

and $\lambda_n = \beta_n/L$ where β_n are the solutions to the transcendental equation

$$\cosh\,\beta_n \cos\,\beta_n + 1 = 0.$$

The corresponding eigenfrequencies are

$$\omega_n = \frac{\beta_n^2}{L^2}\sqrt{\frac{B}{\rho_m h}}. \tag{6}$$

In Fig. 2 the plate deformation is plotted for a sequence of times after the plate has been released from an applied deformation that corresponds to the shape of the eigenmode, Eq. (5), to be simulated. The plate properties used give $m = 2.6\,\mathrm{kg/m^2}$, $B = 4.92\,\mathrm{kN\,m}$, $L = 2\,\mathrm{m}$ and we have chosen $C = 0.01\,\mathrm{m}$. The flexible plate has been discretized to give $N = 100$. Fig. 2 clearly shows that as the plate retains its eigenmode shape and over the cycle of oscillation and recovers its original amplitude. Measured frequencies from these oscillation match the theoretical eigenfrequencies predicted by Eq. (6) within an accuracy (r.m.s. error) of 0.78% for Mode 1 decreasing to 6.73% for Mode 6. These results confirm the integrity of the computational model and its implementation.

2.2. Fluid mechanics

We solve the Navier–Stokes equations in the domain of Fig. 1(b) using a finite-element method written specifically for the channel geometry within which the flexible plate moves. However, the finite-element method chosen and implemented uses standard approaches, and so only an overview is provided here to serve as a summary of its key features. For details, the reader is referred to a standard text such as Bathe (1995), Reddy and Gartling (1994) or Reddy (1993).

We have chosen to discretize the domain using triangular elements with quadratic velocity and linear pressure variations, known as Taylor–Hood elements (Taylor and Hood, 1973). The ensuing block form of the Navier–Stokes equations for the nodal variables of velocity, $u = (u_1, u_2)$, and pressure, p, are

$$M\frac{\mathrm{d}u}{\mathrm{d}t} + C(u)u = D^{\mathrm{T}}p - \frac{1}{\mathrm{Re}}Au, \tag{7}$$

$$D \cdot u = 0, \tag{8}$$

where M, A and D are, respectively, the mass, stiffness and gradient matrices and $C(u)$ is the convection matrix. Time-discretization is applied using an Euler forward scheme and the convection term is handled explicitly by an Adams–Bashforth 3 scheme. Upon re-arrangement of Eq. (8), the final block form of the Navier–Stokes equations is

$$\begin{bmatrix} \frac{1}{\mathrm{Re}}A + \frac{1}{\Delta t}M & 0 & -D_1^{\mathrm{T}} \\ 0 & \frac{1}{\mathrm{Re}}A + \frac{1}{\Delta t}M & -D_2^{\mathrm{T}} \\ -D_1 & -D_2 & 0 \end{bmatrix} \begin{Bmatrix} u_1^{t+\Delta t} \\ u_2^{t+\Delta t} \\ p^{t+\Delta t} \end{Bmatrix} = \frac{1}{\Delta t}\begin{bmatrix} M & 0 & 0 \\ 0 & M & 0 \\ 0 & 0 & 0 \end{bmatrix} \begin{Bmatrix} u_1^t \\ u_2^t \\ 0 \end{Bmatrix}$$
$$- \frac{1}{12}(23C(u^t) - 16C(u^{t-\Delta t}) + 5C(u^{t-2\Delta t})), \tag{9}$$

that permits updated variable values, with superscript $t + \Delta t$, to be found from the velocity field known at earlier times. Note that the convection term on the right-hand side is assembled using the velocity field at three previous times. The choice of time step Δt required for numerical stability is only dependent upon the convection term because in its absence the scheme is implicit. The present Navier–Stokes solver has been validated using a number of standard test cases such as lid-driven cavity and plane channel flows; these are comprehensively reported in Balint (2001).

2.3. Coupled flow–structure system

Full coupling between the structural and flow solutions separately described above is achieved by matching the flow domain and boundary conditions with the vertical displacement, speed and acceleration of the flexible plate. Plate-motion is constrained to be 1-D; thus, the transverse boundary condition is zero velocity on the displaced surface of the

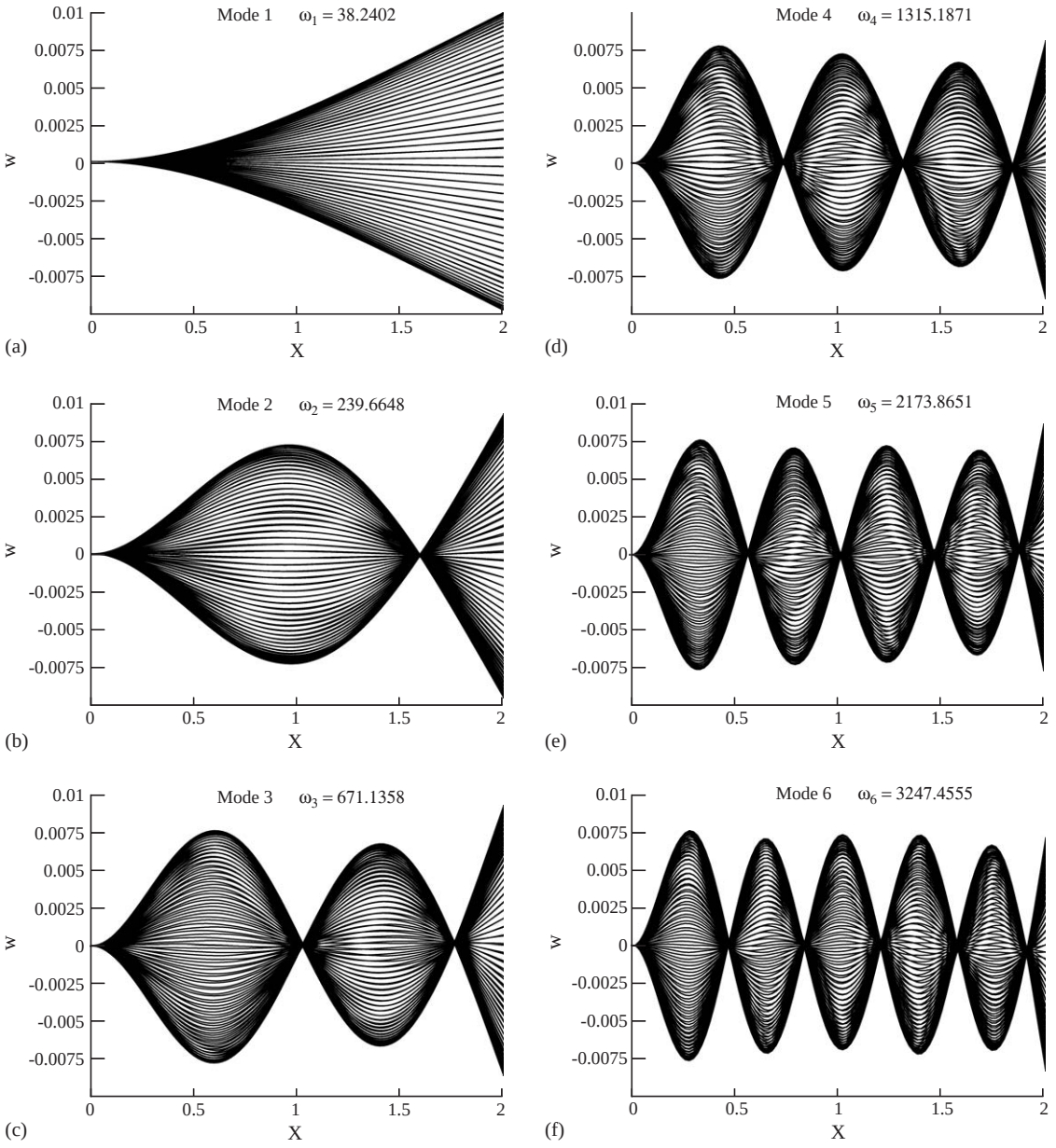

Fig. 2. Deformation-sequences of the simulated first six in vacuo flexible-plate (beam) eigenmodes. Plate data gives $m = 2.6\,\mathrm{kg/m^2}$, $B = 4.92\,\mathrm{kN\,m}$, $L = 2\,\mathrm{m}$ with amplitude scaling constant $C = 0.01\,\mathrm{m}$.

plate. The flow solution obtained from these conditions then provides the pressure distribution on the two sides of the flexible plate that drives its motion.

Plate displacement and flow domain are matched by conducting a boundary-fitting re-mesh at every time-step of system evolution. The no-slip condition on the plate is applied at the displaced position by zeroing the horizontal component of the fluid velocity; this is a linearization based upon small ratios of amplitude to wavelength in the deformation of the plate. Of course, this assumption is already made in the adoption of thin-plate mechanics. In the results that follow we consider the dependence of response upon plate-deformation amplitude to assess the validity of these assumptions. The velocity boundary condition is enforced by setting the vertical component of the flow at the plate boundary to be equal to that of the plate. It is also necessary to match fluid and plate acceleration at this

boundary. Because velocities are matched, all that is necessary to achieve this is to use the same time-step for both the flow and plate solutions. On all of the rigid boundaries both no-slip and no-flux conditions are enforced. At inflow to the channel, uniform flow is prescribed whilst at the outlet boundary the pressure is set to zero and the vertical component of the velocity is set to zero. The effect of this outlet condition is examined in Section 3.1 below.

We remark that the type of coupling described immediately above yields an explicit scheme for the coupled system, not only because the flow solution is explicit in the convection term, but because the solutions for flow and plate motion are sequenced, separated by Δt, as opposed to being strictly concurrent. This can lead to numerical phase shifts between fluid and plate motions that generate artificial energy transmission between the two media. Such phase shifts are clearly dependent upon the choice of Δt and thus we have taken care, by assessing time-step dependence, to ensure that the flutter-type phenomena reported in Section 3.2 are caused by genuine phase shifts between the fluid forcing and the motion of the flexible plate. Another source of error arises from re-meshing the domain at every time step. Elements in the blocks bounded by the flexible plate undergo a change in flow area at each time step and the previously calculated velocities at the nodes are not adjusted. However, the time steps used resulted in a maximum change of 0.8% in element flow-area change and so this systematic error is tightly controlled. Moreover, we have repeated a number of simulations using coarser meshes and have found that the flow–structure physics reported in Section 3 below remains unchanged.

Simulations of the flow–structure interaction require some form of initial condition from which the coupled motion develops. In most of the cases presented herein, the flexible plate has been initially deflected into either the first or second in vacuo mode seen in Fig. 2. The flow field corresponding to the geometry of the statically deflected plate within the selected channel configuration is then computed by the present flow-solution scheme, using time-stepping until the fully developed steady flow is reached. This sets the starting condition for the flow. The plate is then released and computation for coupled plate and flow motions commences.

3. Results

The results reported here identify how the soft palate (cantilevered flexible plate) can be destablized by the fluid flow in each of two channel configurations, the first, Section 3.2, in which both oral and nasal inlets are open and the second, Section 3.3, in which one is blocked. Instability is judged to occur when the overall plate energy shows a sustained increase with time. The energy equation (per unit width) for the plate, in the absence of dissipation, is derived by multiplying Eq. (1) by $\dot{w}$ and then integrating over the plate length to give

$$\frac{\mathrm{d}}{\mathrm{d}t}\left(\underbrace{\frac{1}{2}m\int_0^L \dot{w}^2\,\mathrm{d}x}_{\text{Plate kinetic energy}} + \underbrace{\frac{1}{2}B\int_0^L w_{,xx}^2\,\mathrm{d}x}_{\text{Plate strain energy}}\right) = \underbrace{\int_0^L (-\Delta p)\dot{w}\,\mathrm{d}x}_{\text{Rate of work by fluid},\dot{W}} - \underbrace{d\int_0^L \dot{w}^2\,\mathrm{d}x}_{\text{Dissipation rate},\dot{D}}. \tag{10}$$

We remark here that there is no contribution from the fluctuating shear stress on the flexible plate. This is because plate-motion is constrained to occur solely in the vertical direction. A full nonlinear flexible-plate model would, of course, permit motion in the horizontal direction due to both material extension (or contraction) in that direction and the geometric effects of large-amplitude deformations. However, we might anticipate, based on studies of boundary-layer flows over rubber-like compliant coatings deforming in both vertical and horizontal directions [for example, see Lucey and Carpenter (1995)], that the normal-stress energy production exceeds the viscous dissipation rate of the fluctuating shear stress by an order of magnitude.

For the discretized plate the strain and kinetic energies are, respectively, evaluated using

$$E_s(t) = \frac{1}{2}B\sum_{i=1}^{N}\left[\frac{w_{i+1}-2w_i+w_{i-1}}{\delta x^2}\right]^2\delta x \quad \text{and} \quad E_k(t) = \frac{1}{2}\rho_m h\sum_{i=1}^{N}(\dot{w}_i)^2\delta x, \tag{11a,b}$$

where $\delta x = L/N$ is the distance between mass points in the finite-difference scheme. The total plate energy is $E_t(t) = E_s(t) + E_k(t)$. It is normalized using the deflection—or strain energy input—applied to the plate at the start of the simulation. Hence, the normalized plate energy is defined by

$$\bar{E}_t(t) = \frac{E_t(t) - E_t(0)}{E_t(0)}. \tag{12}$$

Clearly, plate energy grows when the right-hand side of Eq. (10) is positive and this is the case when a positive rate of work exists that exceeds the rate of energy dissipation through structural damping. We also consider the relative

magnitudes of the applied pressure force due to the flow, and the plate's internal force (per unit width); these are respectively given by

$$F_f = \int_0^L (-\Delta p)\,\mathrm{d}x \quad \text{and} \quad F_p = B\int_0^L w_{,xxxx}\,\mathrm{d}x. \tag{13a,b}$$

These are nondimensionalized through division by ρU_{in}^2, where U_{in} is the channel inlet uniform flow speed.

The energy-growth instability criterion is clearly met when $F_f > F_p$ and this indicates a divergence-type of instability. The plate ceases to oscillate and the deformation amplitude grows in a quasi-static manner. However, instability can also occur when $F_f < F_p$, for which oscillatory motion continues. In this case, the energy-growth instability criterion is met by the existence of a phase shift between the fluid pressure, $(-\Delta p)$ and the plate motion, $\dot{w}$ in Eq. (10). This can yield a positive rate of energy transmission from flow to wall—the term $\dot{W}$—that exceeds the dissipation rate $\dot{D}$. This is a flutter instability. Accordingly, in the results that follow, we evaluate energy rates and both flow-induced and internal plate forces in order to identify both the nature and the severity of unstable behaviour.

3.1. System data and discretization

System parameters are based upon known snoring frequencies that lie in the range 30–100 Hz; see Gavriely and Jensen (1993). Correlation between analogue experiments and in vivo measurements, see Huang (1995), suggests that the second mode is responsible for flutter of the soft palate. Accordingly we have chosen thin-plate properties to have elastic modulus, Poisson ratio and specific mass, respectively, given by 880 MPa, 0.3333 and 0.025 kg/m^2 giving an in vacuo second-mode frequency of 100 Hz for a flexible-plate length $L = 8.5$ mm. We use an inspiratory volumetric flow rate of 0.0004 m^3/s, noting that the typical maximal rate is 0.0010 m^3/s; when combined with a typical airway hydraulic diameter of 20 mm this yields a mean inflow speed of $U_{\mathrm{in}} = 1.27$ m/s. The equivalent 2-D duct has a channel height $H = 10$ mm. Throughout this investigation the splitter plate and leading edge of flexible plate are fixed at mid-channel height, $H/2$. These data yield a Reynolds number, Re, of 1512 based on channel height H. We also perform simulations at lower inflow rates to investigate the dependence of system response on Reynolds number. In developing the Reynolds number we use air density and kinematic viscosity values of 1.18 kg/m^3 and 1.68×10^{-5} m^2/s, respectively. The fluid domain has total length 40 mm and the extent of the flow domain upstream of the flexible plate permits the full development of plane Poiseuille flow within the inlet sections for the Reynolds numbers studied. To investigate the dependence of system response on inflow rate, we also perform simulations for $\mathrm{Re} = 756$ ($U_{\mathrm{in}} = 0.64$ m/s) and 378 ($U_{\mathrm{in}} = 0.32$ m/s).

Fig. 3 summarizes the finite-element discretization of the flow domain used to generate the results presented below. Time-step, Δt, was chosen to be 5×10^{-5} s and simulations were typically continued for five cycles of a mode-2-type oscillation (100 Hz in vacuo) to yield a total run time of 0.05 s. Coarser discretizations, in both space and time, were also used to generate results not presented. These confirm that the phenomena presented herein are not artifices arising from inadequate discretization. The flexible plate was discretized using 17 lumped mass points. This number is sufficient to capture, within 2% accuracy, the frequency of the second eigenmode. It will be seen below that it is the first and second eigenmode deformations that dominate instability mechanisms in the flow–structure interaction. We have also investigated the dependency of response upon the channel length downstream of the flexible plate. This parameter is known to influence the inertial load due to the fluid and thereby modify oscillation frequencies of the flexible plate. Variations of ±25% from our selected domain length yield less than a 0.1% change to the frequency of fluid-loaded flexible plate oscillating in mode 2; our results are therefore appropriate to those of an infinite channel downstream of the flexible plate.

3.2. Both inlets open—plate flutter

Fig. 4 shows a sequence of snapshots of the flow field and deformation of the flexible plate over one cycle of oscillation for $\mathrm{Re} = 1512$ in the absence of plate damping. The imposed initial perturbation took the form of the second in vacuo beam (plate) eigenmode with a tip-amplitude ($w_0 = 2$ mm) to channel half-height ratio, $2w_0/\mathrm{H}$ of 0.4, the largest used in our investigation. This sequence provides a qualitative record of the system response. In the grey-scale, the dark-centred oval regions *within* the flow indicate high streamwise components of the flow velocity. Clearly, these regions grow and decay to generate an oscillatory pressure field associated with the plate motion. Fig. 5 shows sequences of plate deformation over the first five cycles of oscillation for three different initial tip-amplitudes, $2w_0/H = 0.1, 0.2$ and 0.4, for each of the Reynolds numbers, $\mathrm{Re} = 378$ and 1512; Fig. 5(f) corresponds to the simulation illustrated by Fig. 4. The thick lines denote the initial (black) and final (dashed grey) deformations of the flexible plate.

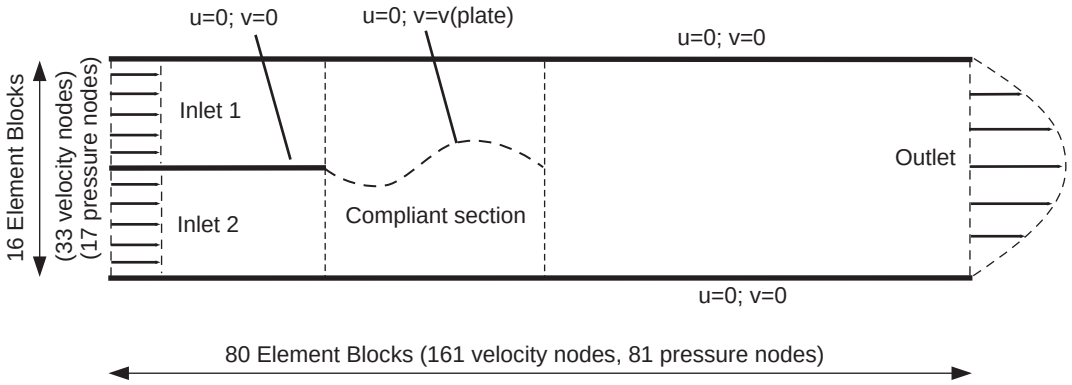

Fig. 3. Schematic of the fluid domain detailing discretization of the finite-element scheme.

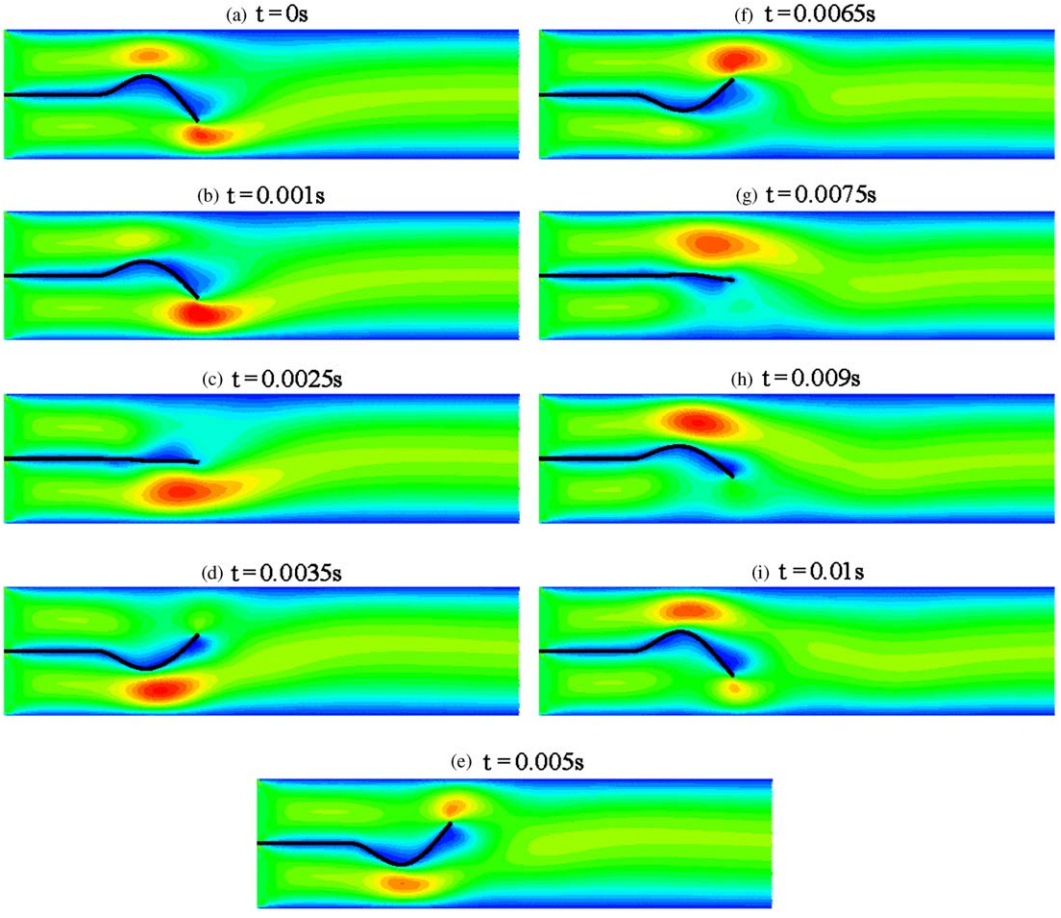

Fig. 4. Sequence of snapshots of the flow field and flexible-plate (thick black line) for both inlets open for air-flow at $\mathrm{Re} = 1512$ illustrating flutter instability. (Colour contours indicate the horizontal component of the air velocity on a spectral scale of light grey (red), indicating high, to dark grey (blue) indicating slow). Plate data is $E = 880\,\mathrm{MPa}$, $v = 0.3333$, $m = 0.025\,\mathrm{kg/m^2}$, $d = 0$ and $L = 8.5\,\mathrm{mm}$ to give a in vacuo second-mode frequency of 100 Hz; the tip-amplitude of the initiating applied mode is $w_0 = 2\,\mathrm{mm}$, giving $2w_0/H = 0.4$.

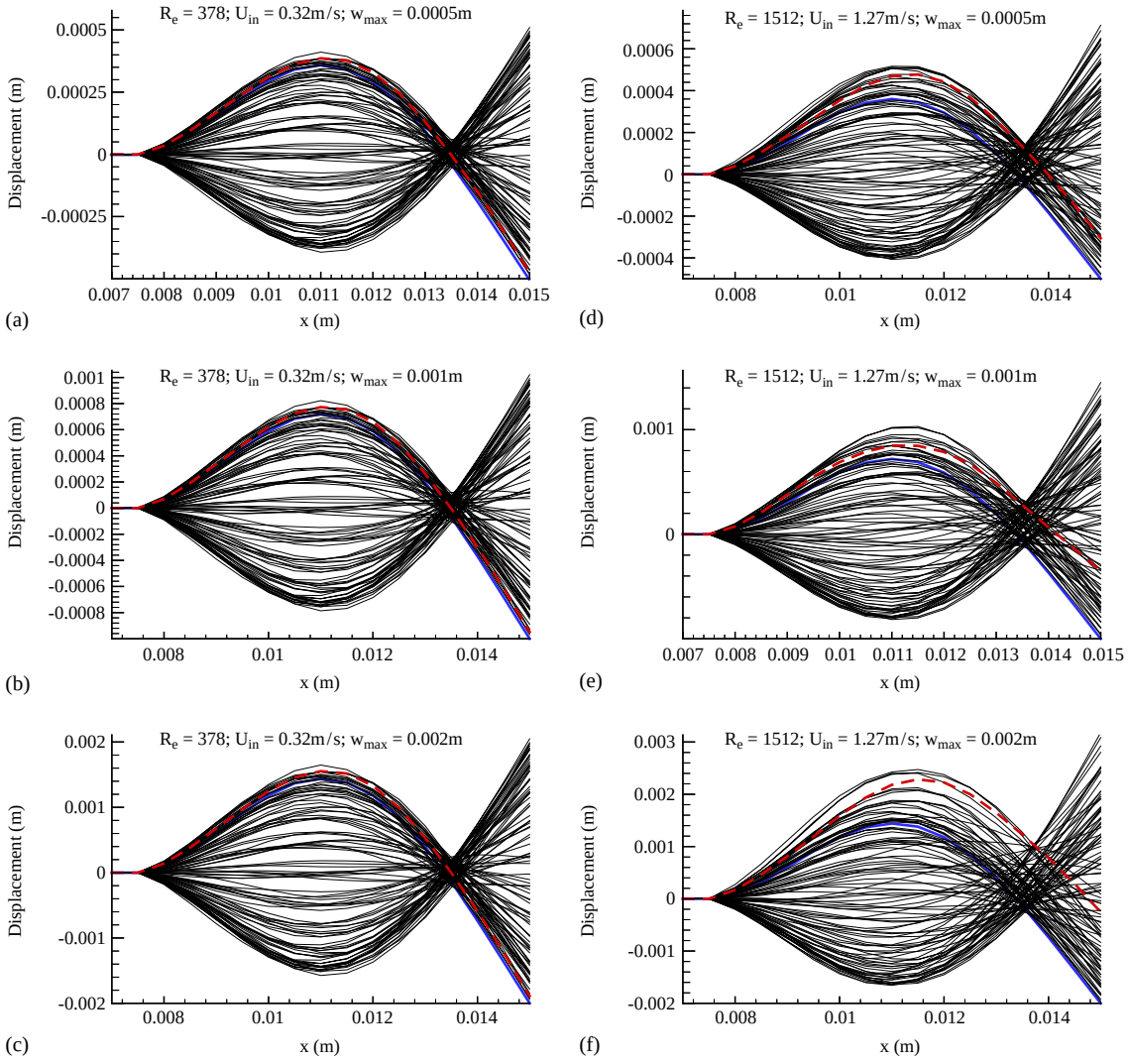

Fig. 5. Sequences of flexible-plate deformation for five cycles of oscillation for (a)–(c) Re = 378 and (d)–(e) Re = 1512, for different tip-amplitudes of the initiating applied mode, $2w_0/H = 0.1$, 0.2 and 0.4. Initial and final deformations are, respectively, marked by thick black (blue) and dashed-grey (red) lines. Both inlets open and flexible-plate data as for Fig. 4.

At the higher Reynolds number the deformation clearly undergoes amplification over the cycle. At the lower Reynolds number, careful inspection of Figs. 5(a–c), also indicates amplitude growth. It is also evident throughout that the amplifying deformation retains its essential second-mode shape and frequency. The present simulations permit other modes to be excited. Their absence in Fig. 5 at these and later times strongly indicates that mode 2 is the critical mode because it has the highest amplification rate for this channel configuration.

We now consider instability in terms of plate-energy growth. Fig. 6(a) shows total work done, W, by the pressure on the plate over the first cycle of oscillation, $t : 0 \rightarrow 0.01$ s, as it varies with Reynolds number. Records for the three different initial amplitudes of Fig. 4 are displayed. In the absence of damping, $\dot{D}$ in Eq. (10), positive $W = \int \dot{W}\,\mathrm{d}t$ means that the plate energy has increased indicating unstable behaviour. Fig. 6(a) then shows that the plate is unstable at all Reynolds numbers in the absence of plate damping and that instability growth rate increases with Reynolds number. The inclusion of energy dissipation by plate damping then yields a critical Reynolds number at which the rate of energy-transfer to the plate first exceeds that at which it is dissipated, i.e. $\dot{W} > \dot{D}$ in Eq. (10). The determination of critical Reynolds number is shown in Fig. 6(b) which was generated by conducting a set of simulations that correspond to the case of $2w_0/H = 0.4$ in Fig. 6(a) but now with structural damping included. In Fig. 6(b) we plot ΔW, the

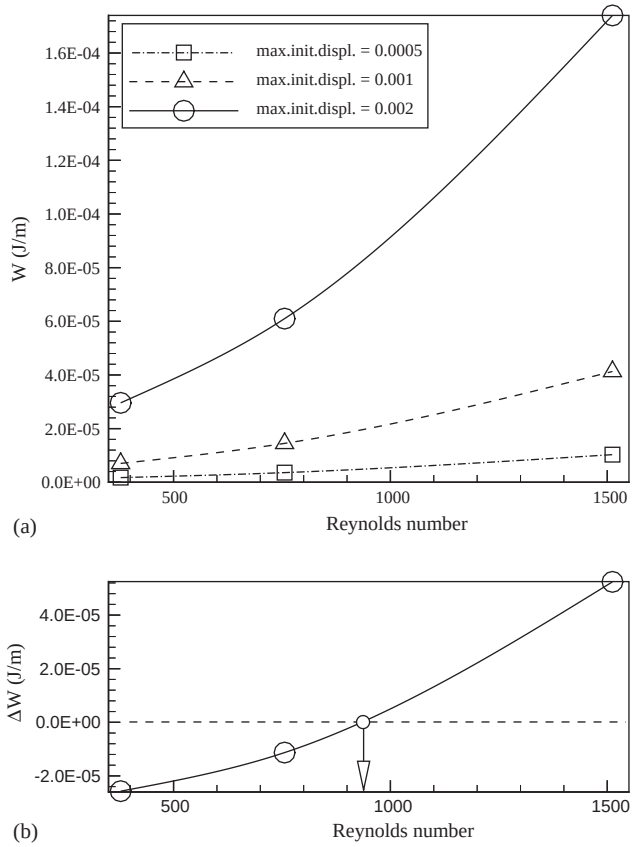

Fig. 6. Variation with Reynolds number of (a) total work done, W, on an undamped plate for different amplitudes of the initiating second-mode shape, and (b) the difference, ΔW, between work done by the pressure forces and dissipation for the case with initial amplitude $2w_0/H = 0.4$ when material damping is included. In all cases the calculation of work is performed over one cycle of plate oscillation, $t : 0 \rightarrow 0.01$ s, with both inlets open and flexible-plate data as for Fig. 4.

integration of the right-hand side of Eq. (10) over one period, having used a damping-coefficient $d = 5\,\mathrm{Ns/m^3}$ chosen for illustrative purposes only. This level of damping reduces the amplitude of the second in vacuo mode by approximately 65% over one cycle of oscillation. The point at which $\Delta W = 0$ gives the critical value of the Reynolds number. We do not attempt to generate meaningful critical Reynolds numbers in this paper because we do not have in vivo data upon which to base and evaluate realistic viscoelastic damping for the soft-palate (plate) material. Nevertheless, Fig. 6(b) shows that it is the balance between work done on the plate by the fluid forces and dissipation that determines the stability threshold. We also remark that, in a more complete model of plate motion, dissipation could also occur through the fluctuating fluid shear stresses on the surface of plate as well as through material damping within the plate.

The flutter instability is therefore caused by irreversible energy transfer from the flow to plate made possible by the phase shift between the pressure and the vertical speed of the plate that yields positive $\dot{W}$ in Eq. (10). This transfer is, of course, spatially dependent. Thus, in Fig. 7 we plot the ratio of energy transfer in the upstream half of the plate, $x : 0 \rightarrow L/2$ to that which occurs in the downstream half, $x : L/2 - L$. This figure shows that the principal contribution to the flutter mechanism occurs near the root of the plate, as opposed to its free end where the motion is most pronounced. This type of awareness will be essential for clinicians seeking to alleviate upper-airway impairment by intervention directed at modifying the properties of the soft palate.

We now consider the quantitative effect of mode amplitude on flutter growth rate. Fig. 8 therefore shows how the normalized plate total energy, $E_t(t)$ defined by Eq. (12) increases with time for three initial tip-amplitudes, $2w_0/H = 0.1, 0.2$ and 0.4, for each of the three Reynolds numbers. The highest and lowest Reynolds numbers are those for which sequences of plate deformations over five cycles were presented in Fig. 5. The very near collapse of these data onto three Reynolds-number curves suggests that the flutter mechanism is essentially independent of plate amplitude. This might

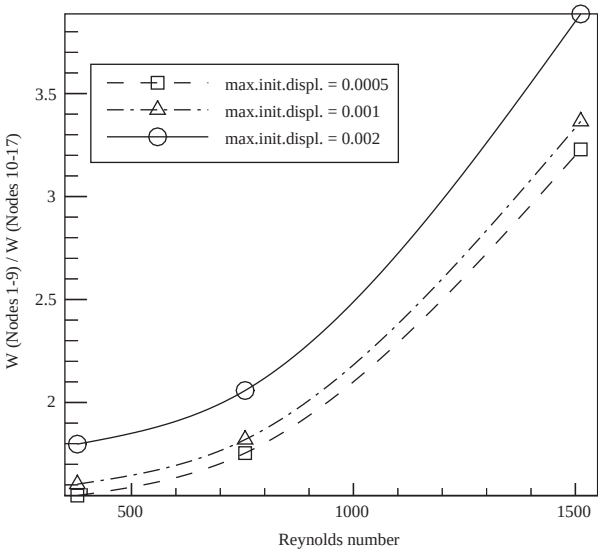

Fig. 7. Ratio of energy transfer in the upstream half of the plate to that occurring in the downstream half as it varies with Reynolds number for different amplitudes of the initiating second-mode shape. Both inlets open and flexible-plate data as for Fig. 4.

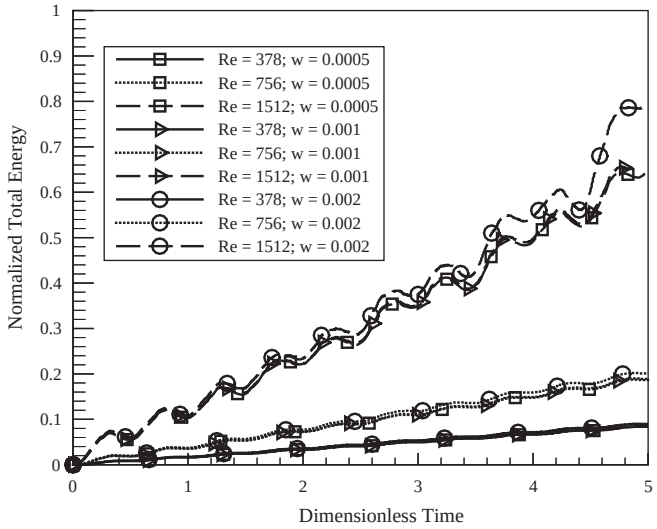

Fig. 8. Evolution of normalised plate-energy for different Reynolds numbers and amplitudes of the initiating second-mode shape. Both inlets open and flexible-plate data as for Fig. 4.

well be expected on the grounds that a linear, 1-D, model of plate mechanics has been used. However, the fluid mechanics is highly nonlinear. What these results then indicate is that our range of $2w_0/H$ remains closer to unbounded flow past a cantilevered plate and that Bernoulli-type effects arising from (oscillatory) channel blockage—such as those modelled by Aurégan and Depollier (1995)—are not responsible for the flutter mechanism herein. We also remark that our ratio of channel half-height to plate length is $H/2L = 0.59$. Guo and Païdoussis (2000) denote this ratio c and their Fig. 8 shows that flutter due to potential flow behaves like that in an unbounded system for the $c = 0.59$ and mass ratio $\mu = \rho_f L/m = 4.01$ in our investigation. Thus, it is flow curvature combined with viscous effects that provide the phase-shifted fluid forcing that feeds the plate flutter in much the same way as the analogous quasi-inviscid study of Huang (1995). This inference is consistent with the result of Fig. 7 showing that the destabilizing energy transfer principally occurs in the upstream part of the plate as opposed to its trailing edge where blockage effects are greatest.

Finally, we consider the possibility that the phase-shift between pressure and plate motion driving the flutter is caused by time-dependent flow-separation from the plate. Fig. 9 shows a sequence of snapshots of the vorticity field over the fifth cycle of oscillation of the simulation that yielded Fig. 4. Close inspection of this figure does not reveal a region of reverse vorticity near the trailing edge of the plate on the side of the plate in an adverse pressure gradient. Vorticity is shed continuously from the plate's trailing edge as the lift on the plate varies through the cycle. Downstream of the plate, vorticity roll-up occurs and these vortices successively impact on the upper and lower walls of the channel where they are dissipated some distance before the downstream end of the flow domain. Further indirect evidence suggests that time-dependent separation is not the cause of the flutter found in the present work. Fig. 8 showed data-collapse of the normalized plate energy for different deformation amplitudes. Clearly, plate curvature is greater for higher deformation amplitude. This would generate a steeper adverse pressure gradient near the trailing edge and earlier separation. Thus, one would then have an energy-transmission mechanism that is dependent upon deformation amplitude. Fig. 8 shows that this is not the case. Thus, the flutter found in the present work is due to phase shifts caused by viscous effects in the attached boundary layers on the two surfaces of the deforming plate. However, for a similar system with a combination of much higher Reynolds number and very-large amplitude deformation, time-dependent flow separation could be a significant phenomenon that contributes to energy exchanges between flow and structure.

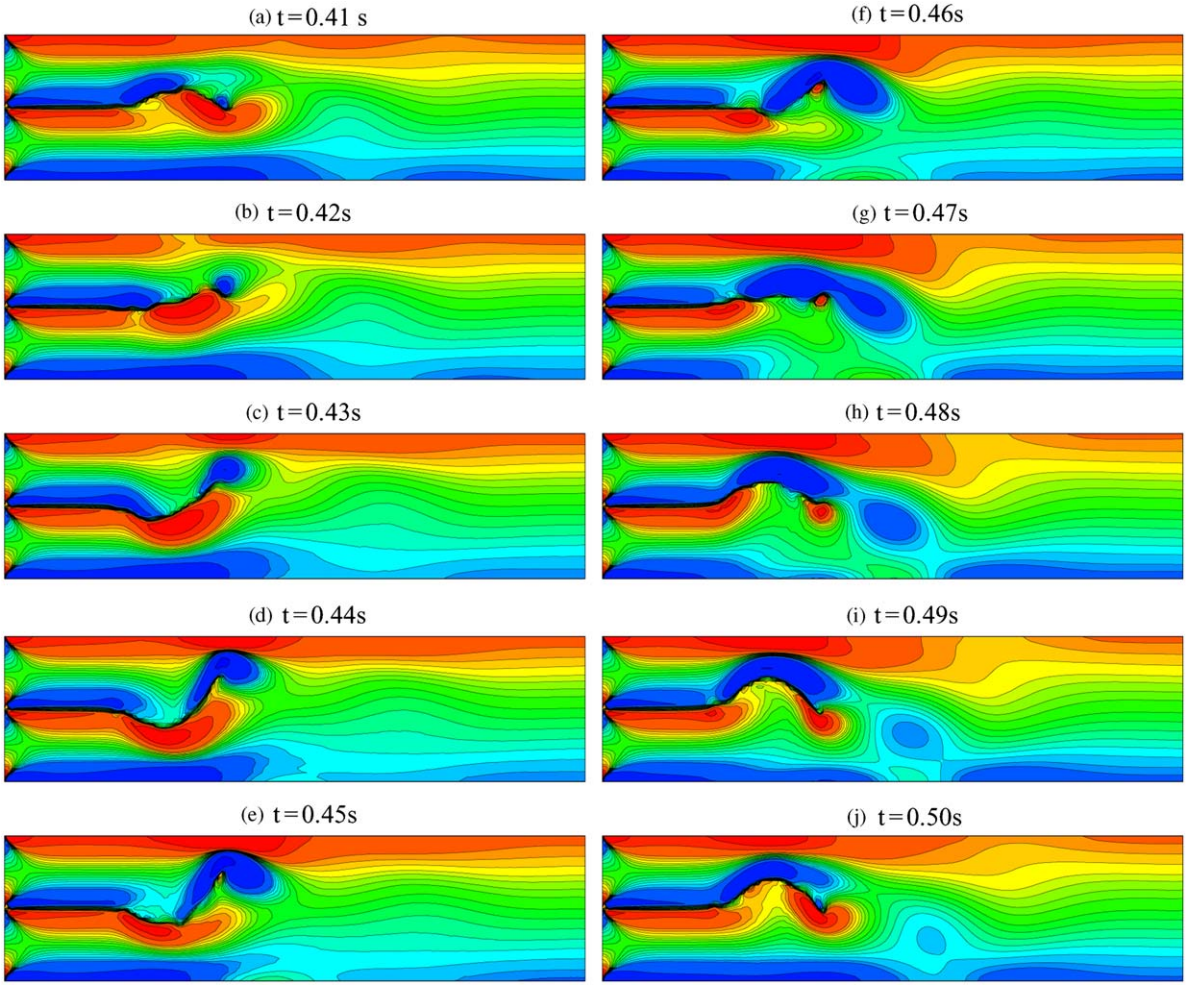

Fig. 9. Sequence of snapshots of the vorticity field corresponding to the to the fifth cycle of the flutter instability seen in Fig. 4. (Greyscale indicates vorticity sign and magnitude on a spectral scale of dark grey (blue), indicating clockwise, to light grey (red) indicating anticlockwise while the lines are contours of iso-vorticity.)

3.3. One inlet blocked—plate divergence

We now turn our attention to the case where either the upper or lower inlet is closed. The position of the splitter plate and flexible plate mounting at a height $H/2$ makes these cases identical. In the results presented here it is the lower channel which has been blocked. We retain the same set of uniform inlet speeds, $U_{\text{in}} = 1.27, 0.64$ and $0.32\,\text{m/s}$, but note that this implies a halving of both volumetric inflow rates and channel Reynolds numbers relative to the two-inlet case studied in Section 3.2.

We first consider the response associated with a plate possessing structural damping, assigning a value $d = 3\,\text{N s/m}^3$ to the damping coefficient. This represents a reduction of the amplitude of the second beam in-vacuo mode from its initial value by approximately 50% over one cycle of oscillation for the plate properties used herein. Fig. 10, with $U_{\text{in}} = 0.64\,\text{m/s}$ (Re = 378), and Fig. 11, with $U_{\text{in}} = 1.27\,\text{m/s}$ ($Re = 756$), each show a sequence of snapshots of the flow field and deformation of the flexible plate. In both cases the flexible plate was initially deformed into the shape of the second in vacuo beam mode with a tip-amplitude $w_0/H = 0.1$. At the lower speed in Fig. 10, the plate can be seen to commence an oscillation while the deformation changes from that of the imposed mode-2 shape to one that is closer to the fundamental mode. In the last snapshot, at $t = 0.45\,\text{s}$, the plate has effectively come to rest and the system remains steady thereafter. The deformation and amplitude of the flexible plate have therefore evolved so that the pressure force due to the flow, F_f, and the plate's internal force, F_p are exactly balanced yielding a static equilibrium for the flow–structure system. In contrast, Fig. 11 illustrates instability. Although the behaviour is similar to that seen in Fig. 10, at this higher inflow speed the flexible plate does not come to rest but its amplitude in the final quasi-mode-1 shape continues to grow until shortly after the final frame at $t = 0.046\,\text{s}$ it will impact the upper wall. Thus at this flow

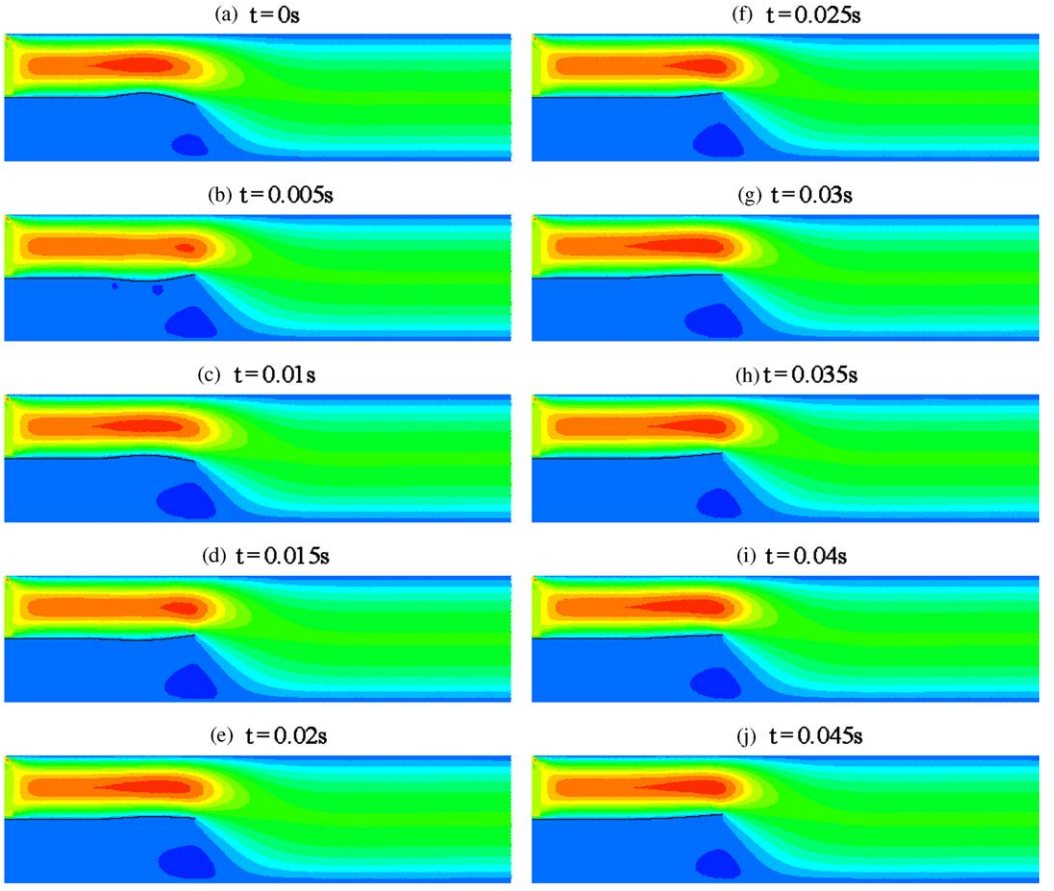

Fig. 10. Sequence of snapshots of the flow field and motion of a damped flexible-plate (thick black line) with lower inlet blocked and upper inlet flow speed $U_{\text{in}} = 0.64\,\text{m/s}$ (Re = 378). One inlet open and plate data as for Fig. 4 except that $d = 3\,\text{N s/m}^3$. (Colour contours indicate the horizontal component of the air velocity on scale from predominantly light grey (red) being high, to dark grey (blue) being low.)

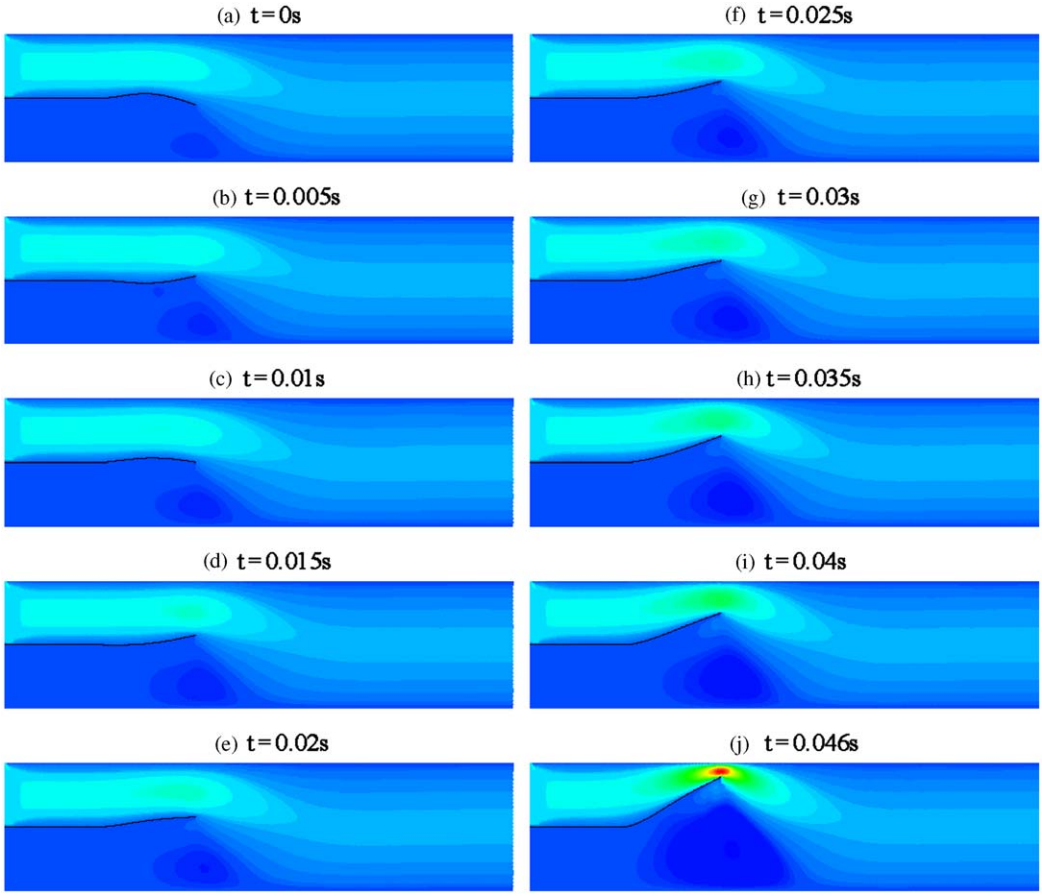

Fig. 11. Sequence of snapshots of the flow field and motion of a damped flexible-plate (thick black line) with lower inlet blocked and upper inlet flow speed $U_{\text{in}} = 1.27\,\text{m/s}$ (Re = 756) illustrating divergence instability. All other data as for Fig. 10.

speed, once the instability mode has evolved, $F_f > F_p$ for all subsequent amplitudes and continued growth ensues. This is a divergence instability.

The simulations of Figs. 10 and 11 are represented quantitatively in Fig. 12 where we show the evolution of flexible-plate strain (E_s), kinetic (E_k) and total ($E_t(t) = E_s(t) + E_k(t)$) energies with time. At the lower flow speed, Fig. 12(a) shows a rapid decay from the initial value associated with the imposed mode 2 until the total energy asymptotes to a low, but nonzero, value corresponding to the final plate deformation seen in Fig. 10(j). In contrast, Fig. 12(b) (note the different scale on the vertical axis to that in Fig. 12(a)) at the post-critical flow speed shows an initial energy decay associated with the attenuation of the imposed mode-2 starting deformation, followed by rapid growth as the flexible plate assumes the shape of the unstable divergence mode.

The results presented so far may appear to suggest that structural damping is essential for the plate to lose its stability through divergence. We will now show that this is not so, but that without damping both divergence and flutter instabilities co-exist. Setting the damping coefficient to zero, we repeat the simulations of Figs. 10 and 11. Fig. 13 shows sequences of plate deformation for each of the same two inflow speeds, $U_{\text{in}} = 0.64$ and 1.27 and for three different initial tip-amplitudes, $2w_0/H = 0.1, 0.2$ and 0.4. Again the initial excitation took the form of the second beam mode. At the lower flow speed, Figs. 13(a–c), sustained mode-2 oscillations continue. Amplification of this mode is discerned by contrasting the initial (black) and final (dashed grey) deformations. This, we will see is caused by the same flutter mechanism that prevailed in the two-inlets-open configuration. However, an overall shift upwards of the centre of oscillation has occurred because the dominant flow is over the upper surface that leads from the open inlet. At the higher inflow speed that generates Figs. 13(d,e), noting the change in axis scaling between corresponding initial tip-amplitude figures, the response is very different. The plate deformation is seen to evolve into a shape that has mode-1 as its greatest contribution and rapid amplification through divergence occurs. Thus the rôle of damping in the simulations

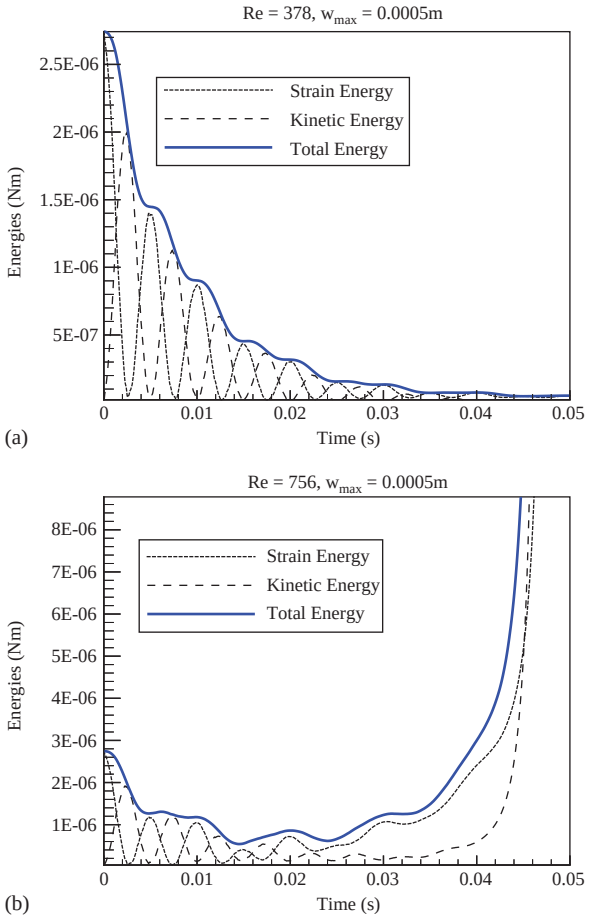

Fig. 12. Evolution of flexible-plate energy for one inlet blocked and open inlet flow speed (a) $U_{\text{in}} = 0.64\,\text{m/s}$ (Re = 378), and (b) $U_{\text{in}} = 1.27\,\text{m/s}$ (Re = 756). All other data as for Fig. 10.

of Figs. 10 and 11 was to overcome the flutter instability at the lower flow speed and Reynolds number and ultimately yield the static equilibrium that obtains from the plate-energy equation (10) when $\dot{D} = \dot{W}$ on the right-hand side. The elimination of flutter by damping then shows that the flow speed is sub-critical with respect to divergence. At the higher flow speed, divergence instability is seen to set in—Figs. 11 and 13(d–f)—irrespective of whether damping is present or not.

To confirm that the instability seen in Figs. 11 and 13(a–f) is indeed divergence, we consider the relative magnitudes of the pressure force due to the flow, F_f, and the plate's internal force, F_p, as defined by Eqs. 13(a,b). In Fig. 14 we contrast the magnitude of the forces for exactly the same undamped simulations recorded in Fig. 13. At the lower flow speed, Figs. 14(a–c), it is seen that $|F_p| > |F_f|$ throughout and this confirms sub-critical behaviour with respect to divergence. It is also evident that both $|F_p|$ and $|F_f|$ show oscillatory growth indicating unstable behaviour. This is caused by the flutter instability present in the absence of damping that, like the two-inlets-open case described in Section 3.2 is caused by energy transfer from flow to plate through the source term $\dot{W}$ on the right-hand side of the plate-energy equation (10). At the higher flow speed, Figs. 14(d–f) show near balance between $|F_p|$ and $|F_f|$ at early times when the imposed mode-2 deformation predominates. However, at later times, when the divergence mode has formed it is clearly seen that $|F_f| > |F_p|$ and this is the mechanism for the rapid growth of divergence instability. Because F_f scales with $\rho\bar{U}^2$, where $\bar{U}$ is the mean flow speed in the channel, then the divergence onset is principally dependent upon flow speed. This is in contrast with the flutter mechanism revealed in Section 3.2 for which a critical Reynolds number exists because viscous effects are responsible for the phase shift between pressure field and plate motion that causes the dynamic destabilization. Finally, we remark that the most unstable divergence mode that evolves is one that minimizes the curvature of the plate deformation. For an effectively one-sided loading this is the configuration that minimzes $|F_p|$,

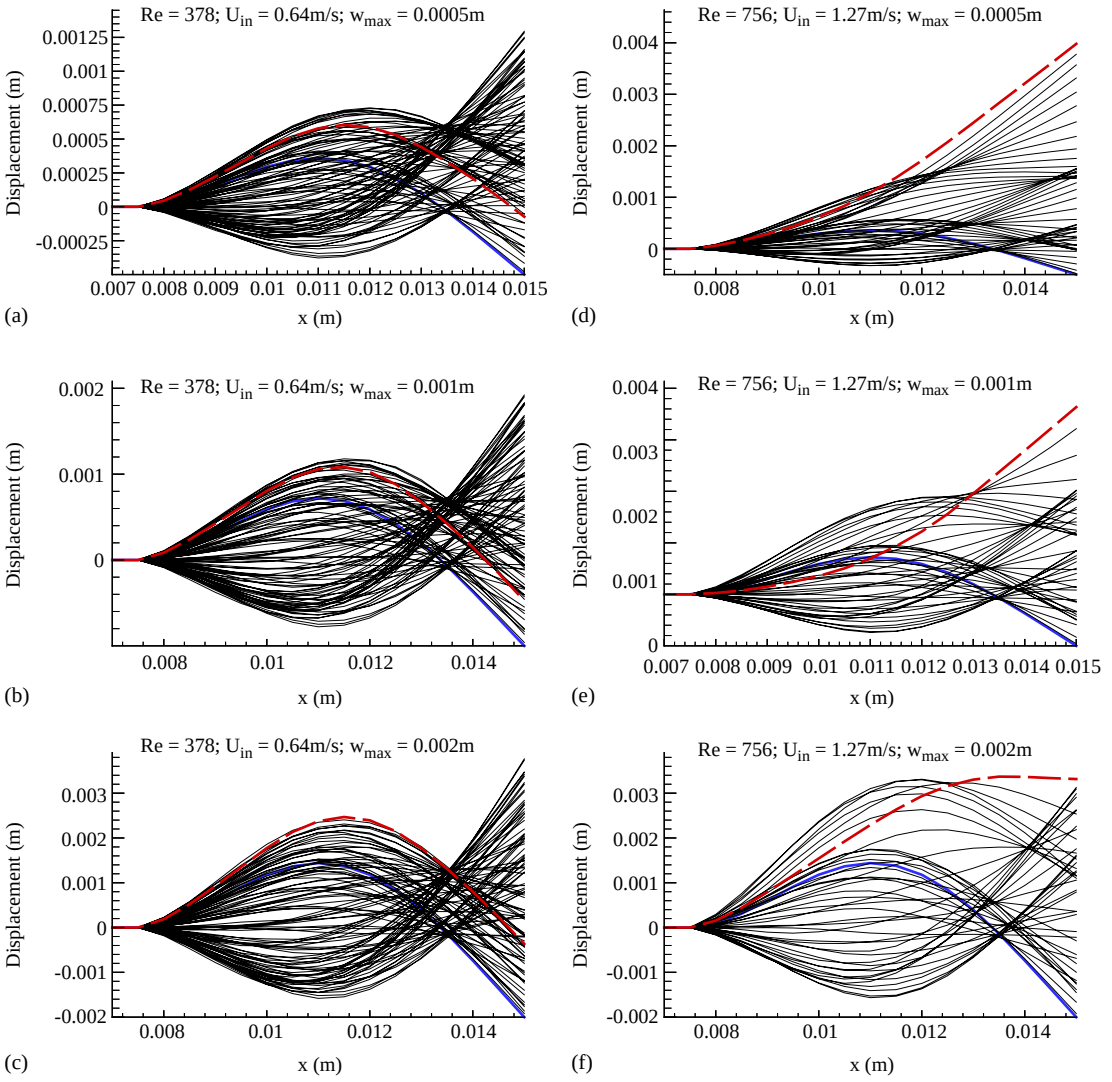

Fig. 13. Sequences of undamped flexible-plate deformation for one inlet blocked $U_{in} = 0.64\,\mathrm{m/s}$ (Re = 378) (a)–(c) and $U_{in} = 1.27\,\mathrm{m/s}$ (Re = 756) (e)–(f) for different tip-amplitudes of the initiating applied mode, $2w_0/H = 0.1$, 0.2 and 0.4. Initial and final deformations are respectively marked by thick black (blue) and dashed-grey (red) lines. Flexible-plate data as for Fig. 4.

hence restorative plate stiffness, while permitting the maximization of the destabilizing hydrodynamic stiffness that is principally generated at the plate tip due to the blockage effect between plate and upper wall of the channel.

4. Concluding remarks

A computational model has been developed to simulate the motion of an arbitrarily deforming cantilevered flexible plate embedded in viscous plane-channel flow. An investigation has been conducted to identify the mechanisms by which the flexible plate can become unstable for two configurations that are characteristic of the human upper-airway system when breathing impairment occurs through snoring and sleep apnoea.

When both upper and lower channels (airways) are open, the plate loses its stability through flutter. The underlying mechanism for the instability is irreversible energy transfer from flow to plate due to a phase difference between the fluid pressure and the plate motion. Instability sets in beyond a critical Reynolds number when this energy transfer exceeds the rate of plate-energy dissipation.

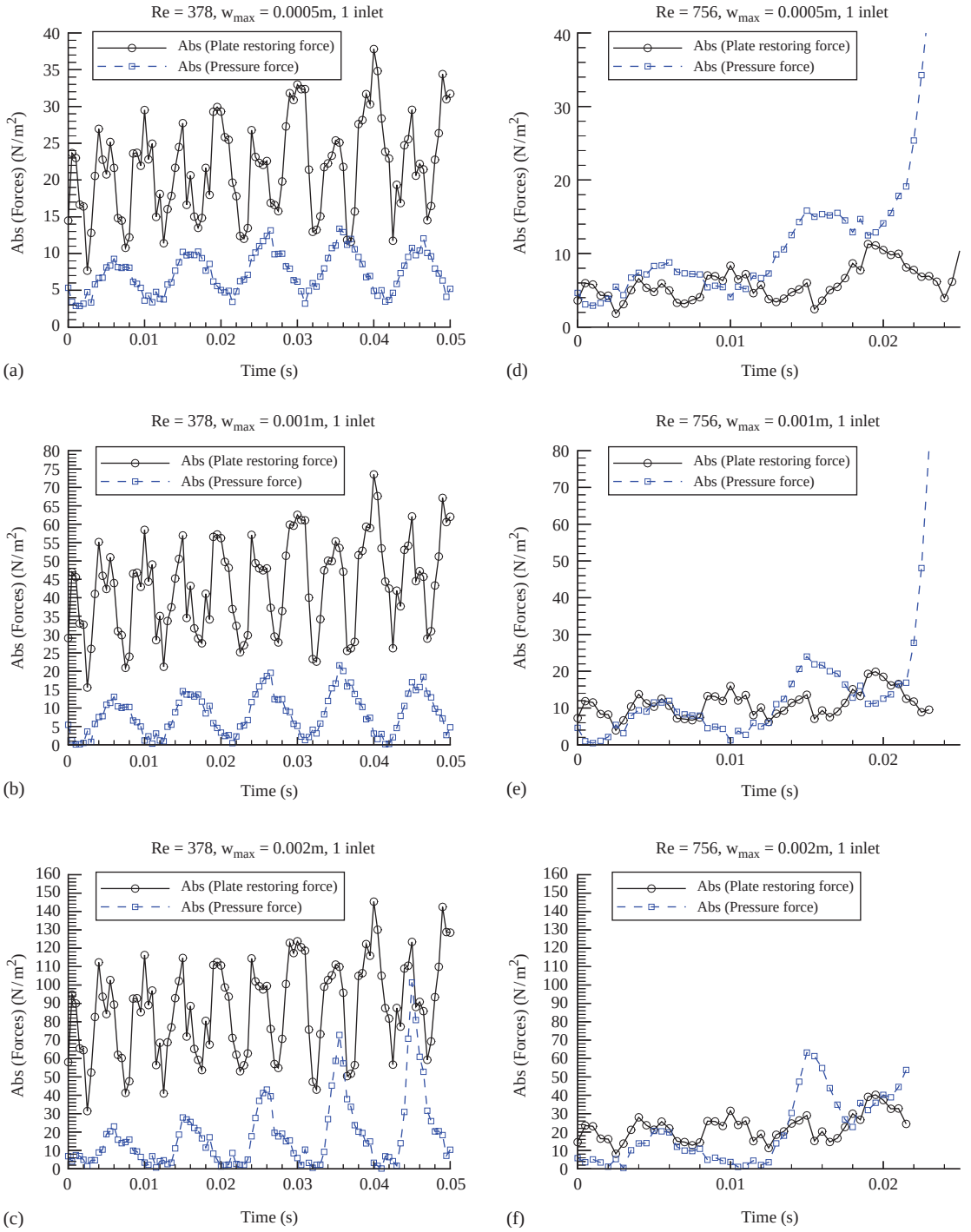

Fig. 14. Variation with time of magnitudes of fluid-pressure and plate-restorative forces at inlet flow speeds (a)–(c) $U_{in} = 0.64\,m/s$ (Re = 378), and (e)–(f) $U_{in} = 1.28\,m/s$ (Re = 756), for different tip-amplitudes of the initiating applied mode, $2w_0/H = 0.1$, 0.2 and 0.4. One inlet is blocked and the plate is undamped; flexible- plate data as for Fig. 4.

When one airway is blocked, the principal means of destablization is divergence which sets in at a flow speed beyond which the magnitude of the fluid-pressure force exceeds the restorative structural forces in the plate. Structural damping promotes pure divergence by facilitating the formation of a critical deformation shape. However, for very low values of damping at flow speeds below that of divergence onset, flutter may exist and at higher flow speeds a combination of flutter and divergence instability mechanisms can be responsible for oscillatory growth. In such cases, the plate deformation largely comprises fluctuating combinations of both first and second modes of plate deformation.

The present work has modelled unsteady laminar flow up to Reynolds numbers that are very close to transitional. Maximum inspiratory flows, combined with geometries that vary between individuals, could lie in the turbulent range of Reynolds numbers. Thus, we may speculate as to whether the basic instability mechanisms uncovered here carry across to turbulent channel flow. The flutter instability has been shown to occur through phase shifts between the oscillating pressure field and plate motion. Moreover, it seems that, for the representative geometries used in this paper, partial-blockage effects in the channel are not implicated. Thus, the instability mechanism is similar to the Huang (1995) flutter for an unbounded fluid domain. Although Huang used a potential-flow solution, it was the enforcement of the Kutta condition, required by plate finiteness, that effectively generated the phase shifts. The deforming flexible plate is a variable-lift thin aerofoil and the Kutta condition reflects the (changing) lumped bound vorticity that is the sum of the spatially distributed vorticity located in the boundary layers on the upper and lower sides of the aerofoil. This is true whether the boundary layers are laminar or turbulent. In our study these boundary layers are actually modelled and the Kutta condition is satisfied automatically. We therefore see the phase shift as being generated by the action of the viscous boundary layers and it is reasonable to expect that the same effect will hold for a turbulent boundary layer. The present phase-shift flutter type of instability is well-known in laminar boundary-layer flow over compliant coatings: the travelling-wave flutter (TWF) elucidated in, for example, Carpenter and Garrad (1986) and Lucey and Carpenter (1995). Like the flutter found in this paper, the critical Reynolds number for TWF is fundamentally dependent upon the level of damping in the compliant-coating material. Gad-el-Hak (1986) has shown that TWF also occurs when the boundary layer is turbulent. Thus, we would expect the same type of flutter instability to exist for turbulent channel flow although, like the complaint-coating counterpart, the critical Reynolds number for the instability could be very different. The divergence instability we have found for the single-inlet configuration is most likely to occur for turbulent channel flow because it is not principally a product of viscous effects. Instead it owes itself to the high hydrodynamic stiffness, dependent on flow speed as opposed to Reynolds number, caused by partial blockage to the upper channel in a predominantly one-sided flow. However, these predictions clearly warrant investigation given the Reynolds-number range of upper airway flow.

We recognize that the system studied herein represented by Fig. 1(b) is a radically simplified version of that in the human upper airway. In particular, our use of a 2-D rectilinear geometry appears to be a coarse approximation. Thus, in Fig. 15 we present a preliminary calculation of the mean flow in an upper-airway system of typical geometry and which corresponds the anatomical sketch of Fig. 1(a). Fig. 15(a) shows the computational domain. Oral inlet, nasal inlet and pharynx exit channels have, respectively, heights 3.8, 4.4 and 4.9 mm and all have width 10 mm. The distance from the plane of nasal inlet to the pharynx is 47 mm; this provides a metric for other dimensions in the system modelled. The flow domain was meshed using approximately 170 000 tetrahedral elements with mesh biasing near channel walls. The system geometry was created using Unigraphics NX 2.0 while the fluid computations were carried out using the commercial finite-element code CFDesign Version 7. Two examples of the calculated mean flow are given in Figs. 15(b) and (c); these show the velocity magnitudes at the mid-section of the system. Fig. 15(b) shows the mean flow when both oral and nasal inlets are open through which uniform air-flows of 1 m/s enter each inlet while Fig. 15(c) shows a case with one inlet (the oral) blocked and a 2 m/s air-flow through the nasal entry. Both cases suggest that the mean flow over the hard and soft palate is quite reasonably modelled by plane Poiseuille flow whereas the most pronounced effects of curvature on the mean flow occur in the pharynx just downstream of the soft-palate trailing edge. This suggests that the mean flow used in our investigations yields instability mechanisms that would most probably be found in the flow–structure dynamics of the human upper airway.

Finally, an enhanced representation of the biomechanical system needs to include the variation with time of the geometric system seen in Fig. 15(a). This is particularly important in the pharynx, where the tube cross-section varies markedly with time through the breathing cycle. Furthermore, the temporal variation of the pressure-driven flow rate that characterizes human inhalation needs to be modelled. Modelling a pressure driven flow in this system is a particularly challenging task because asymmetries between upper and lower channels will generate different unsteady impedances and thus different flow rates through each channel. In the present work, we considered only the most extreme case of inlet-channel asymmetry for which the blocked channel impedance is trivially known to be infinite. We therefore contend that the flutter and divergence mechanisms that we have described are likely to feature albeit modified quantitatively by the many added complexities that exist in the dynamics of the actual upper-airway system.

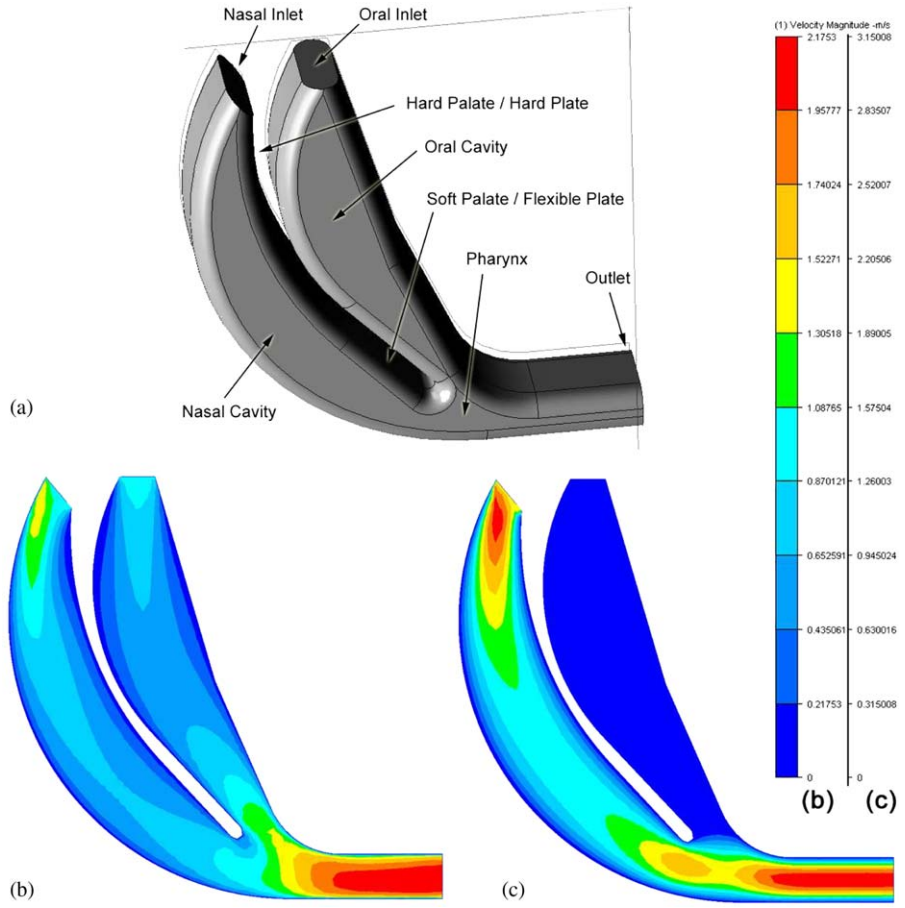

Fig. 15. Calculated mean-flow field in a 3-D representation of the upper-airway flow system: (a) scale diagram of the system, and velocity magnitudes at mid-section for (b) both inlets open with uniform flow at 1 m/s through each, and (c) oral inlet blocked with uniform flow at 2 m/s through the nasal inlet. (Colour contours indicate magnitude of air velocity on scale from predominantly light grey (red) being high, to dark grey (blue) being low.)

Acknowledgements

The authors wish to acknowledge the support of the University of Warwick and Curtin University Technology, the latter for hosting Dr. Balint as a visiting scholar, that permitted this work to be undertaken. The work of this paper is not related to any ongoing research at the Jet Propulsion Laboratory, where Dr. Balint is now employed, nor at the California Institute of Technology. The authors also express their gratitude to Mr. G.A.Tetlow (Curtin University of Technology) who performed and post-processed a number of the simulations.

References

Aittokallio, T., Gyllenberg, M., Polo, O., 2001. A model of a snorer's upper airway. Mathematical Biosciences 170, 79–90.

Aurégan, Y., Depollier, C., 1995. Snoring: linear stability analysis and in-vitro experiments. Journal of Sound and Vibration 188, 39–53.

Balint, T.S., 2001. Dynamics of the upper airway. Ph.D. Thesis, University of Warwick, UK.

Bathe, K.-J., 1995. Finite-element Procedures. Prentice-Hall, Englewood Cliffs, NJ.

Carpenter, P.W., Garrad, A.D., 1986. The hydrodynamic stability of flow over Kramer-type compliant surfaces, Part 2: flow-induced surface instabilities. Journal of Fluid Mechanics 170, 199–232.

Gad-el-Hak, M., 1986. The response of elastic and viscoelastic surfaces to a turbulent boundary layer. Journal of Applied Mechanics 53, 206–212.

Gavriely, N., Jensen, O.E., 1993. Theory and measurement of snores. Journal of Applied Physiology 74, 2828–2837.

Guo, C.Q., Païdoussis, M.P., 2000. Stability of rectangular plates with free side-edges in two-dimensional inviscid channel flow. Journal of Applied Mechanics 67, 171–176.

Huang, L., 1995. Flutter of cantilevered plates in axial flow. Journal of Fluids and Structures 9, 127–147.

Huang, L., Ffowcs Williams, J.E., 1999. Neuromechanical interaction in human snoring and upper airway obstruction. Journal of Applied Physiology 67, 1759–1763.

Kornecki, A., Dowell, E.H., O'Brien, J., 1976. On the aeroelastic instability of two-dimensional panels in uniform incompressible flow. Journal of Sound and Vibration 47, 163–178.

Lucey, A.D., Carpenter, P.W., 1995. Boundary layer instability over compliant walls: comparison between theory and experiment. Physics of Fluids 7, 2355–2363.

Lucey, A.D., Cafolla, G.J., Carpenter, P.W., Yang, M., 1997. The nonlinear hydroelastic behaviour of flexible walls. Journal of Fluids and Structures 11, 717–744.

Nowacki, W., 1963. Dynamics of Elastic systems. Chapman and Hall, London.

Pierce, R.J., Worsnop, C.J., 1999. Upper airway function and dysfunction in respiration. Clinical and Experimental Pharmacology and Physiology 26, 1–10.

Reddy, J.N., 1993. An Introduction to the Finite Element Method, second ed. McGraw-Hill, New York.

Reddy, J.N., Gartling, D.K., 1994. The Finite Element Method in Heat Transfer and Fluid Dynamics. CRC Press, LLC, London.

Taylor, C., Hood, P., 1973. A numerical solution of the Navier–Stokes equations using the finite-element technique. Computers and Fluids 1, 73–100.

Young, T., Palta, M., Dempsey, J., Skatrud, J., Weber, S., Badr, S., 1992. The occurrence of sleep-disordered breathing among middle aged adults. New England Journal of Medicine 328, 1230–1235.